Unraveling the Dynamics of Moisture Transport during Atmospheric Rivers Producing Rainfall in the Southern Andes

Dipjyoti Mudiar[1,2], Roberto Rondanelli[1,2*], Raul A. Valenzuela[2,3] and René D. Garreaud[1,2]

[1]Department of Geophysics, Universidad de Chile, Santiago, Chile

[2]Center for Climate Resilience Research, Universidad de Chile, Santiago, Chile

[3]Institute of Engineering Sciences, Universidad de O'Higgins, Rancagua, Chile

*Corresponding author: ronda@dgf.uchile.cl

Key Points:

- We calculate the moisture transport budget of 50 events of zonal atmospheric rivers over the Pacific that reach South America.
- Horizontal convergence of tropical and subtropical air masses is the primary source of water vapor in atmospheric rivers.
- Following a lagrangian column, precipitable water is roughly conserved along the river, except near landfalling.

Abstract: Atmospheric rivers (ARs) are known to produce both beneficial and extreme rainfall, leading to natural hazards in Chile. Motivated to understand moisture transport during AR events, this study performs a moisture budget analysis along 50 zonally elongated ARs reaching the western coast of South America. We identify the convergence of moist air masses of tropical/subtropical origin along the AR as the primary source of vertically integrated water vapor (IWV). Over the open ocean, moisture convergence is nearly balanced by precipitation. The advection of moisture along the AR, although smaller compared to mass convergence, significantly increases toward the landfalling region. The near conservation of IWV over the open ocean, observed by tracking a Lagrangian atmospheric column along the ARs, is the explanation behind the seemingly tropical origin of ARs in time-lapse visualizations of IWV.

Plain language summary:

Imagine atmospheric rivers (ARs) as massive, flowing rivers in the sky, but instead of water, they carry vapor from the ocean. When these "sky rivers" travel and hit the Andes Mountains in South America, they can cause a lot of rain and snow to fall. This precipitation is often good because it helps fill reservoirs and water crops. However, sometimes there's too much rain, leading to floods and landslides, which can be dangerous. Over the ocean, the amount of water vapor these atmospheric rivers pick up is almost exactly balanced out by the rain that falls from them. As these atmospheric rivers get closer to South America, the movement of moisture along the river, though generally less significant than the gathering of moist air, becomes more pronounced. This means that as the atmospheric river approaches the land, it starts carrying more moisture towards its destination. We were able to see this process in action by following a moving 'slice' of the atmosphere (a Lagrangian atmospheric column) as it travels along the path of the atmospheric river. This helped us understand how atmospheric rivers maintain their water content as they move. It also shows why atmospheric rivers seem to originate from tropical areas when we look at them in time-lapse images of water vapor.

1 Introduction:

Atmospheric rivers (AR) are transient, narrow, and elongated channels in the atmosphere that are known to transport water vapor and heat poleward from the tropics (Zhu & Newell, 1998). In Central Chile, ARs contribute about 50% of the annual rainfall (Viale et al., 2018) and they are also responsible for extreme rainfall events when water vapor is intercepted by the steep Andes orography, creating hazards such as floods and landslides (Rutllant et al., 2023; Valenzuela et al., 2022; Valenzuela & Garreaud, 2019). Considering that these ARs have to cross through a large gradient of sea surface temperature from the Central Pacific towards cold coastal waters (e.g. Garreaud et al., 2001) local contribution from water vapor is limited, so one expects water vapor to be transported from remote tropical and subtropical moisture sources, especially during extreme episodes. However, the relative importance of advection from remote sources and local moisture convergence in moisture transport during AR is not entirely clear. For instance, Dacre et al. (2015) postulate that the primary source of water vapor in an AR in the North Atlantic is the local moisture convergence induced by surface cyclones, as opposed to the direct transport from the tropical and subtropical regions. In contrast, studies such as Stohl et al. (2008) showed that a substantial amount of moisture could be transported from tropical and subtropical sources during an AR. The notion of direct poleward transport of moisture from tropical or subtropical sources within an AR is also supported by other studies (Bao et al., 2006; Guan et al., 2013). An analysis of extratropical precipitating systems associated with landfalling ARs by Sodemman and Stohl (2013) reveals that poleward moisture transport frequently occurs from the contribution of more than one cyclone aligned with an upper tropospheric jet.

Analyzing the water vapor budget is a key method for understanding atmospheric mechanisms, as highlighted in various studies (Dacre et al., 2015; Guan et al., 2020; Luo & Tung, 2015; Norris et al., 2020). Previous analyses of water vapor budgets of ARs are mostly focused on the leading edge of the AR or different sectors across an AR over the ocean (Dacre et al., 2015; Guan et al., 2020). However, the moist processes occurring inside and along the AR channel largely appear to affect not only the moisture transport over the ocean but also the intensity and duration of landfalling precipitation (Luo & Tung, 2015; Michaelis et al., 2021). As Sodemann and Stohl (2013) and others have noted, an AR is a phenomenon with a scale that surpasses that of a single synoptic-scale cyclone. The planetary scale of an AR becomes apparent when observing a time-lapse visualization of the IWV field over the days leading up to the arrival to the continent, where water vapor from the deep tropics seem to be advected towards the coast over thousands of kilometers. Budgets of water vapor restricted to a specific region within an AR may fail to capture this planetary scale.

In this study, we calculate and analyze AR's moisture budgets considering a novel pseudo-Lagrangian framework. The adopted methods for the moisture budget analysis and data used have been discussed in section 2. The results of the analysis are presented in section 3 comprising a case study followed by the climatological analysis of 50 ARs. The main findings are summarized in the Discussion and Conclusion section .

2. Data and Methods:

The ARs considered in this study are identified based on a global AR detection algorithm included in the AR Tracking Method Intercomparison Project, ARTMIP (Guan & Waliser, 2015). In this study, by visual inspection, we have selected only 50 ARs that made landfall with a dominant zonal orientation over the period 1980-2023.

Zonal ARs tend to be warmer and produce larger orographic enhancement , so are more prone to cause landslides and flooding (Garreaud, 2013; Valenzuela & Garreaud, 2019).

Figure 1 depicts the time evolution of the IWV bands for one of such a zonally elongated ARs, which made landfall in CS Chile on 23 June 2023. An enhanced IWV band is observed to migrate towards CS Chile from 96 hours till the time of landfall. The landfalling time of the AR (hereafter t=0) is identified as the hour when the IWV band reaches the landmass with substantial enhancement in mean precipitation (>10 mm/day) over the study domain (Fig. 1e). Along with the IWV band in Figure 1, the time evolution of 27 trajectories (depicted as white curves) from time t=0 (06 UTC 23 June 2023) is also shown. This ensemble of 27 backward trajectories is calculated from NCEP global reanalysis data using the HYSPLIT trajectory model (Draxler & Rolph, 2010). Each ensemble member corresponds to slightly different initial conditions obtained by offsetting the meteorological data by a fixed grid factor. The initial starting height of the trajectory is 3000 m, well above the boundary layer, with an initial point located at 37°S, 72°W. Among these trajectories, we select the one that has the higher IWV along the trajectory (shown in Fig.1 as a black solid curve) for the budget calculation. The water vapor budgets are calculated considering $5^{o}\times5^{o}$latitude-longitude boxes (to encompass the entire width of the AR) that move backward along this selected trajectory. This process of selection of the trajectory of budget calculation is repeated for all the 50 ARs.

Moisture budget terms are calculated every 6 hours along the trajectory using the meteorological fields obtained from the fifth-generation European Center for Medium-Range Weather Forecasts (ECMWF) reanalysis data sets, ERA5 at $0.25^{o}\times 0.25^{o}$ km horizontal resolution (Hersbach et al., 2020). The *IWV* budget is a balance

between the tendency of *IWV*, vertically integrated water vapor transport ($\vec{IVT}$) convergence, evaporation, E (kg m^{-2} s^{-1}), and precipitation, P (kg m^{-2} s^{-1}) and can be expressed as (e.g. Guan et al., 2020)

$$\frac{1}{g}\frac{\partial}{\partial t}\int_{p_t}^{p_s} q dp = -\nabla\cdot\vec{IVT} + E - P. \quad (1)$$

Here, $p_s = 1000\,hPa$, $p_t = 300\,hPa$, g (m s^{-2}) is gravitational acceleration, q (kg kg^{-1}) is specific humidity, and t(s) is time.

The first term on the right is the convergence of $\vec{IVT}$ and can be further decomposed into three components. So equation (1) can be rewritten as

$$\frac{1}{g}\frac{\partial}{\partial t}\int_{p_t}^{p_s} q dp = -\frac{1}{g}\int_{p_t}^{p_s}\left(\vec{V}\cdot\nabla q + q\nabla\cdot\vec{V}\right)dp - \frac{1}{g}q_s\vec{V}_s\cdot\nabla p_s + E - P \quad (2)$$

Here $-\vec{V}\cdot\nabla q$ represents the horizontal advection of water vapor with $\vec{V}$(ms^{-1}) being the horizontal wind, $q\nabla\cdot\vec{V}$ is the water vapor-weighted mass convergence, and $q_s\vec{V}_s\cdot\nabla p_s$ is a surface term (usually much smaller than the other two components and hence will not be considered further). While the terms related to the specific humidity are instantaneous, the precipitation and evaporation terms are calculated as time means over a 6-hour interval, so we do not expect a perfect balance in equation (2) as explained in *Guan et al*. (2020). However, the mean value of the residue is considerably smaller than the other budget terms (Figure S2).

As the selected trajectories for the 50 AR considered here might exhibit distinct spatio-temporal evolution (see Figure S1), before evaluating the climatological moisture budgets for all these 50 AR, we attempt to understand the moisture budgets in one case study presented next.

3. Results

3.1 A Case Study, 23 June 2023

Before discussing the water vapor budgets, it is important to know the mean synoptic conditions for the zonal AR, since the strength, orientation, and thermodynamic properties of a landfalling AR are known to be influenced by the prevailing synoptic conditions over the ocean (e.g. Garreaud, 2013). A zonally elongated band of high IWV reaches the coast of Chile on June 23rd 2023 (Fig. 1e), associated with a NW-SE quasi-stationary midlatitude trough (see Fig. S2) and a subtropical anticyclone centered at around 25ºS and 90ºW. Surface circulation shows that a large surface cyclone moves slowly centered at about 130ºW at -96 h (Fig. S2e) and at about 110ºW at the landfalling time (Fig. S2h). We also note the presence of a zonally oriented jet streak at the upper levels that migrates towards the coast from -96h to landfalling and whose maximum exceeds 80 ms^{-1}, centered at about 40ºS and 90ºW at landfalling time (Figure S2h). The zonal character of the AR becomes evident only during landfalling and from about 90ºW to 70ºW (Fig. 1e) —otherwise, the poleward migration of the IWV plume is evident from 72 hours before landfall to about 24 hours before landfall (Figs. 1b-d). This AR exhibits a similar synoptic condition as the mean synoptic condition of all the 50 ARs, the evolution of which will be discussed further in

section 3.2.

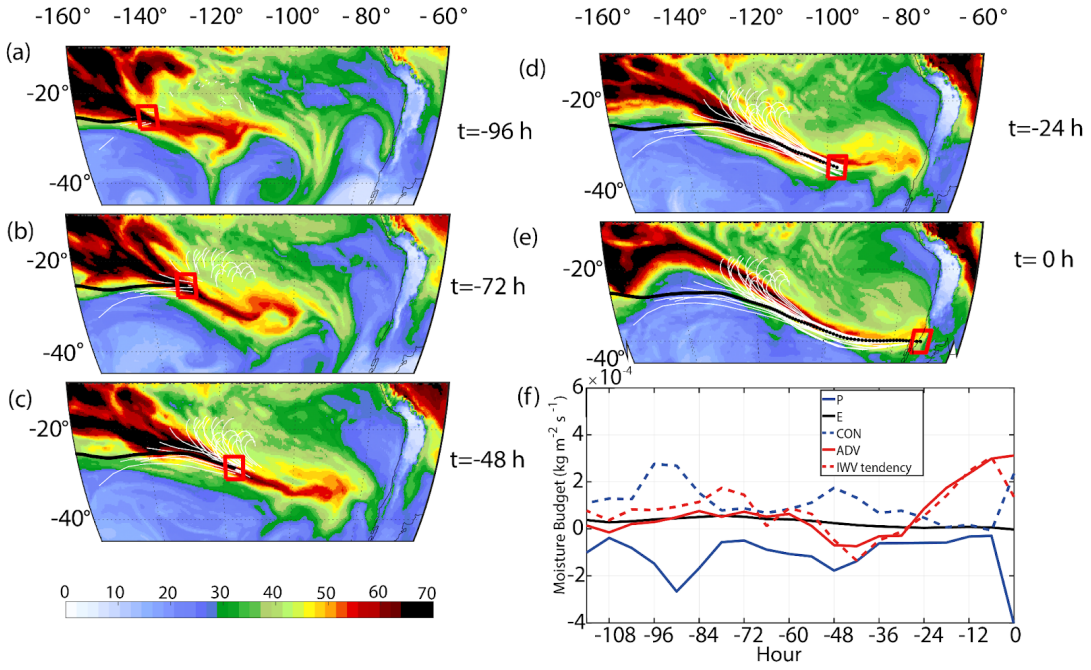

Figure 1: (a-e) Integrated water vapor (IWV) for the case study of 23 June 2023 (time before landfalling is indicated on the right). White curves are the 27 backward trajectories from -108 h to the time corresponding to each of the panels. The solid black trajectory is the trajectory selected for budget analysis. Red boxes indicate the atmospheric column where budget calculations were performed (f) Moisture budget terms (kg $m^{-2}s^{-1}$) for this AR. The terms 'P', 'E', 'CON', 'ADV', indicate domain averaged precipitation, evaporation, convergence, and advection respectively along the IWV tendency terms. The budgets are calculated at 6 hour intervals along the trajectory. The '0 hr' in the x-axis indicates the landfalling time.

Figure 1f shows all the budget terms for this AR at every 6-hour interval. The mass convergence component (CON) of the IVT convergence is positive all along the AR with two prominent maxima: one at -96 hours and one at -48 hours. There is also a

substantial reduction of the convergence between -36 and -6 hours and then an abrupt increase over the landfalling region (-6 to 0 hours). A further decomposition of the 'CON' term into their zonal and meridional components (Figure S3) indicates that these two maxima over the Pacific can be attributed to the horizontal convergence of northerly air masses into the AR. The moisture-loaded air masses coming from a broad region in the tropics and subtropics enter into the AR with the area between the tropical anticyclone and a subtropical cyclone acting as a funnel (see e.g. Figs.1a, S2a-b) related to the maximum of convergence at t=-96h). The mass convergence at lower levels along the AR produces enhanced upward motion, condensation, and precipitation. The depletion of moisture in an atmospheric column along the AR by precipitation (P) is represented by the negative sign convention. Notice that precipitation is in a near balance condition with the mass convergence term at each time along the trajectory(Fig. 1f). The sharp enhancement in precipitation near the landfalling region is produced by the Andes' orographic lifting of the AR. The evaporation (E) component is small and positive all along the AR and decreases towards the colder coastal waters. The advection component of the IVT convergence is generally smaller than the mass convergence term over the open ocean but remains positive except between -50 to -30 hours, where negative advection appears associated with a relative maximum of IWV centered at around 110ºW. The advection term exhibits a significant enhancement near the coast from -30 hours to landfalling The IWV tendency shows positive values suggesting local moistening along the AR, except again between -50 to -30 hours, consistent with the sign of the advection term. The IWV tendency and moisture advection tend to closely follow each other. As the AR advances towards the coast, the advection acts to moisten previously dry regions over the ocean. Once the AR is

established, advection is reduced because of the diminished moisture gradient near the coast.

One important observation from the along-AR budget analysis is the conspicuous difference in moisture transport mechanism over the open ocean and near the landfalling region. While the AR over the open ocean is maintained by moisture-loaded mass convergence into the channel with enhanced PW, transport of moist air mass by advection along the AR dominates near the coast towards the landfalling region. Although the mass convergence term reduces substantially near the coast (from times -24h to -6h), it remains positive for this AR and exhibits a sharp increase over the landfalling region (from -6h to landfalling). As the AR reaches the landmass, mass convergence occurs due to at least two processes: one is the frictional change from ocean to land which may cause horizontal convergence over the landfalling region and the second is the deceleration of the zonal flow due to the topographical barrier. The reduction in mass convergence near the coast (before -6 hours) may be the cause of the reduction in IWV value near the coast as seen in Figure 1d. The sharp enhancement in the advection term towards the landfalling region from -30 hours may be attributed to two possible causes:

a) The relative reduction in precipitation in this time interval may cause an increase in the zonal moisture gradient (notice, for instance, the large moisture gradient along the axis of the river between 90ºW and 80º W in Figure 1d).
b) The merging tropical air masses will transport heat to the AR channel, warming the AR channel ahead of the zone of convergence. Warming the channel by heat advection will increase the saturation vapor pressure, allowing the atmospheric column to hold more moisture and produce larger

advection. Also, this warming may enhance the meridional temperature gradient along the AR, thereby enhancing the zonal wind through thermal wind balance and further increasing advection.

The observed enhanced moisture advection and positive (smaller) mass convergence produce a large enhancement in the IVT convergence over the landfalling region which results in orographic ascent and heavy to extreme precipitation. In this case study, precipitation accumulation in the period between 22nd June and 26th June 2023 ranged from 200 to 800 mm in the piedmont stations around 36ºS causing severe flooding and the rise and overflow of most of the rivers in the region (Garreaud, 2023).

3.2 Water Vapor Budget Climatology along 50 Zonal ARs

The mean synoptic conditions and the time evolution of 50 ARs is shown Figure 2 every 24 hours intervals. Originating in the central Pacific subtropics (20ºS 140ºW), a conspicuous IWV band exhibiting a diagonal shape oriented from northwest to southeast is shown in Fig. 2a-d. A sharp depletion of the IWV toward the coast is noticeable, consistent with the observed reduction in mass convergence near the coast as shown in the case study above. The presence of a trough in midlatitudes and an anticyclone in the subtropics is indicated by the 300 hPa geopotential height contours and the mean sea level (msl) pressure (Figure 2e-h). The eastward propagation and strengthening of the zonally oriented upper level (300 hPa) jet streak is also evident in Figure 2(e-h). The mean 500-hPa omega velocity in Figure 2h shows two main regions of enhanced updraft: one near the continent, likely associated with the topography , and another one centered at 30ºS, 115ºW. This region of enhanced ascent occurs in the equatorward entrance quadrant of the jet streak and coincides with the position of the

trajectory roughly between -72 to -48 hours.

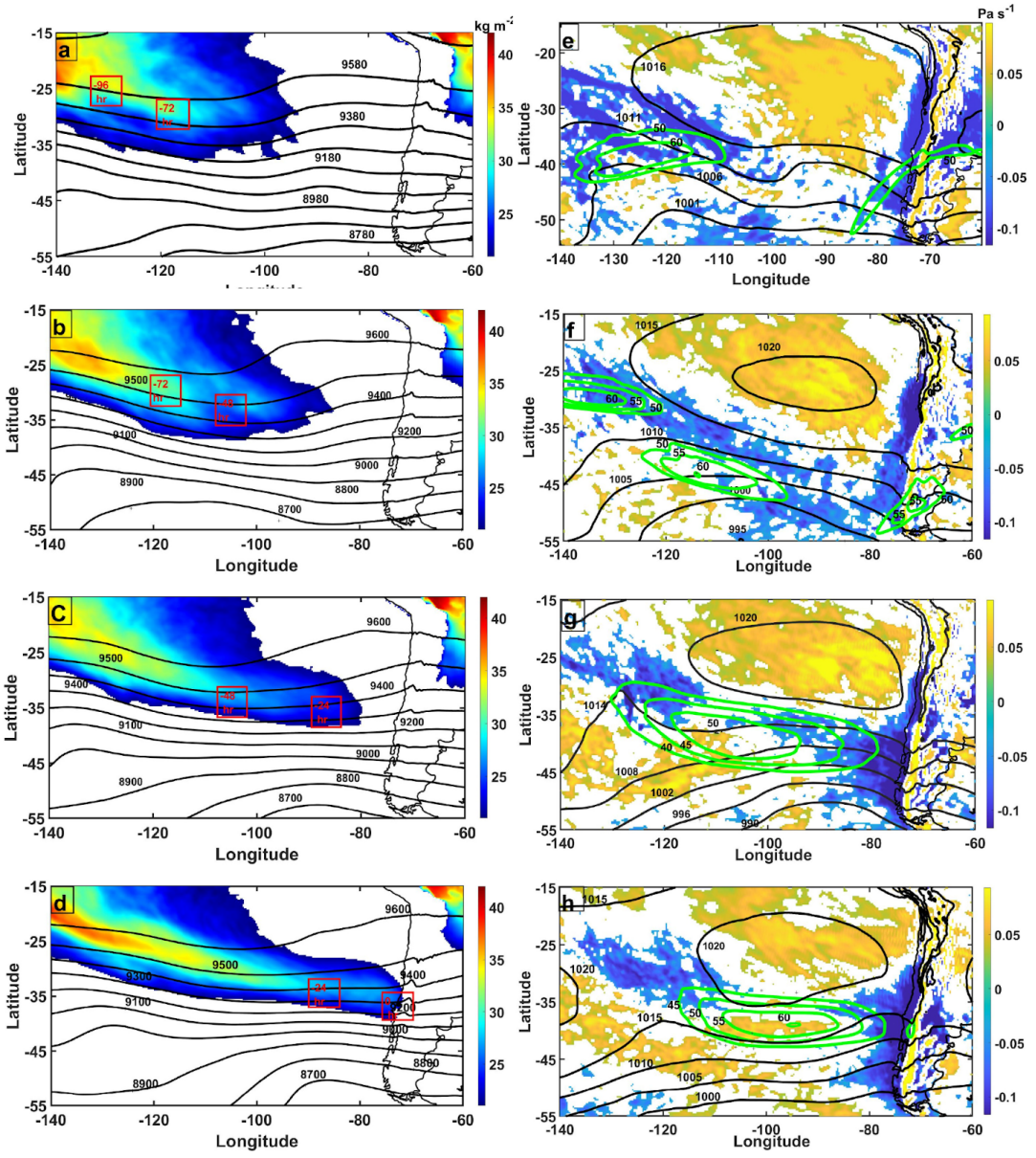

Figure 2: The time evolution (24-hour interval) of mean synoptic conditions for the 50 ARs. All the fields are obtained from ERA5. (a-d) Integrated water vapor (IWV) (shaded) (kg m^{-2}) and 300-hPa geopotential height (contour) (m). The red boxes indicate the approximate position of the air column along the mean trajectory at time steps shown inside the box. (e-h) 500-hPa Omega velocity in pressure coordinate (shaded), 300-mb vector wind (green contour) (m s^{-1}), and the mean sea level pressure (solid

black contours). The panels a-e, b-f, c-g and d-h correspond to the time intervals indicated in the red boxes.

We now look at the composite value of the water vapor budget terms along the 50 ARs, neglecting the small evaporation term. The mean mass convergence term exhibits positive values along the ARs (Figure 3a). A large enhancement in mean moisture convergence is evident between -72 to about -36 hours, in the main region of ascent identified previously. The trajectory analysis suggests that at this time the AR's leading edges are located over the ocean between -140° to -90° W (see Figure S1), where they get fed by the convergence of moist air mass coming from the tropics and subtropics. The convergence of moisture-loaded air masses into the AR produces large upward motion and precipitation as indicated by the precipitation curve, which almost entirely balances the moisture convergence. A positive correlation ($R^2 = 0.65$) between the mass convergence and corresponding precipitation along ARs (see Figure S4) suggests that mass convergence is the primary source of IWV and hence precipitation along the ARs. The mean advection (Figure 3b) is an order of magnitude smaller than the mean mass convergence and sometimes even negative except near the landfalling region where it becomes significant, albeit large variability among the ARs considered. As advection primarily happens inside and along the AR channel, processes inside the AR such as convergence, precipitation, and rain evaporation might have a large influence on the moisture gradient along the ARs and hence on advection causing large AR to AR variability. The mean along-AR *IWV* tendency curve also shows significant variability among the ARs.

Adding the *IWV* tendency and the advection term, we obtain the lagrangian rate of change of the *IWV* ,

$$\frac{D(IWV)}{Dt} = \frac{\partial\,(IWV)}{\partial t} + \vec{V}\cdot\nabla(IWV). \qquad (3)$$

As seen in Fig. 3c this term is small ($\frac{D(IWV)}{Dt} \lesssim 1\ mm\ day^{-1}$) relative to the typical daily mean *IWV* values (~35 *mm*) along these ARs. This suggests that *IWV* is roughly conserved following the Lagrangian atmospheric column along the ARs, except close to the coast. While precipitation effectively balances the IWV from mass convergence (see Figure 3a), the contribution from advection is smaller or sometimes negative (also see *Norris et al* (2020)). This near conservation of *IWV* over the ocean explains why one sees the AR as a continuum object coming from the tropics in the time-lapse visualization of IWV. Near the landfalling region, both mass convergence and the advection show a large increase, resulting in a large enhancement in *IVT* convergence. A close association between *IVT* convergence and precipitation (R^2=0.79) over the landfalling region (Figure 4d) indicates that ARs associated with stronger IVT convergence tend to produce stronger precipitation.

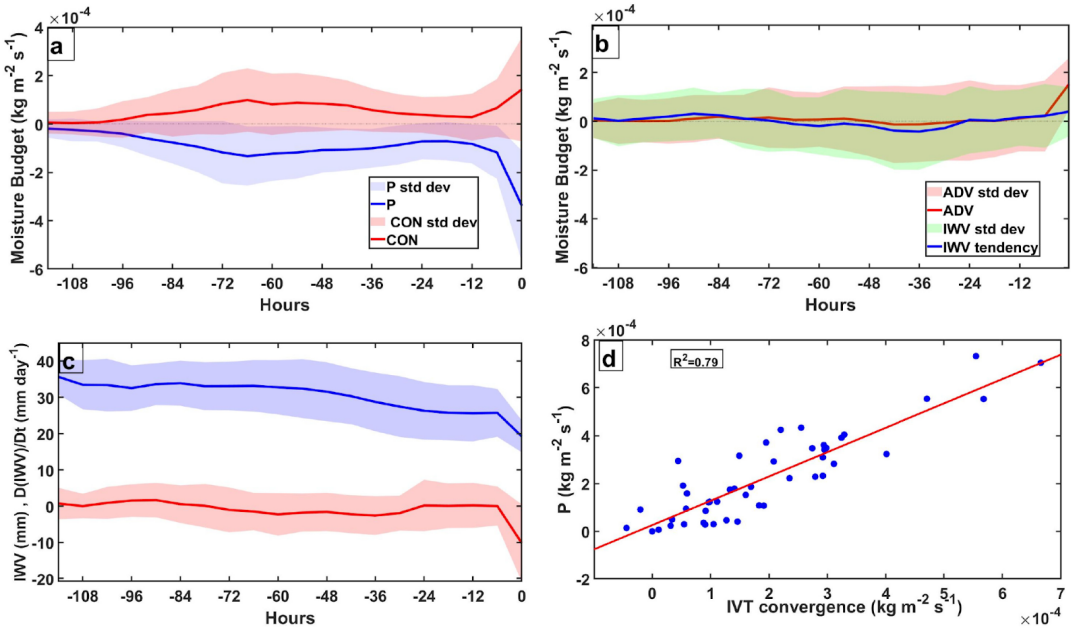

Figure 3: Mean moisture budget for the 50 AR (a) The mean precipitation,' P', and the mean mass convergence, 'CON'. (b) The mean advection term 'ADV' and mean the

IWV tendency. (c) The daily mean integrated water vapor (*IWV*, mm, red curve) and the rate of change of *IWV* ($\frac{D(IWV)}{Dt}$, mm/day, blue curve) following the trajectories. The shaded areas in each plot represent the standard deviation corresponding to each curve. (d) Scatter plot of Integrated water vapor transport (IVT) convergence and precipitation at the land-falling region for all 50 ARs. The red line indicates the best linear fit.

4. Discussion and Conclusions

In this study, we have performed water vapor budget analysis considering 50 zonally elongated ARs using a novel pseudo-Lagrangain method. The analysis of a case study reveals that tropical/subtropical moisture-loaded air masses in the form of bands of enhanced IWV converge into the AR over the open ocean. Expanding the original "river" analogy we can think of an AR as *maintained by "tributaries" which fed the river through moisture convergence over a large tropical and subtropical catchment area. The river "loses" almost the same amount of water that it receives from moisture convergence to precipitation (an actual river has infiltration over the river bed) whereas "streamflow" is roughly conserved following a river parcel*. Mass convergence reduces substantially near the coast again increasing at the landfalling time. The advection of moisture is smaller relative to the mass convergence (sometimes negative) over the open ocean and shows significant enhancement near the coast and towards the landfalling region. At a later time, when the ARs are established over the continent, the moisture gradient along the AR will be much reduced. This process will make advection smaller at the coast while moisture convergence due to orography will maintain precipitation. Our climatological results over 50 zonally elongated ARs support the results by Dacre et al. (2015) that point to the mass convergence as a primary source of water vapor within ARs. However, the converging air masses into the AR appear to be of

tropical/subtropical origin, not necessarily originating in the neighborhood of the ARs. The main contribution of mass convergence observed for these ARs over the open ocean is associated with the equatorward edge of a relatively large-scale cyclonic circulation (see Figure 4), similar to the region of convergence found by Campos and Rondanelli (2023). This convergence also appears to be further enhanced by secondary circulations in the equatorward entrance region of a jet streak.

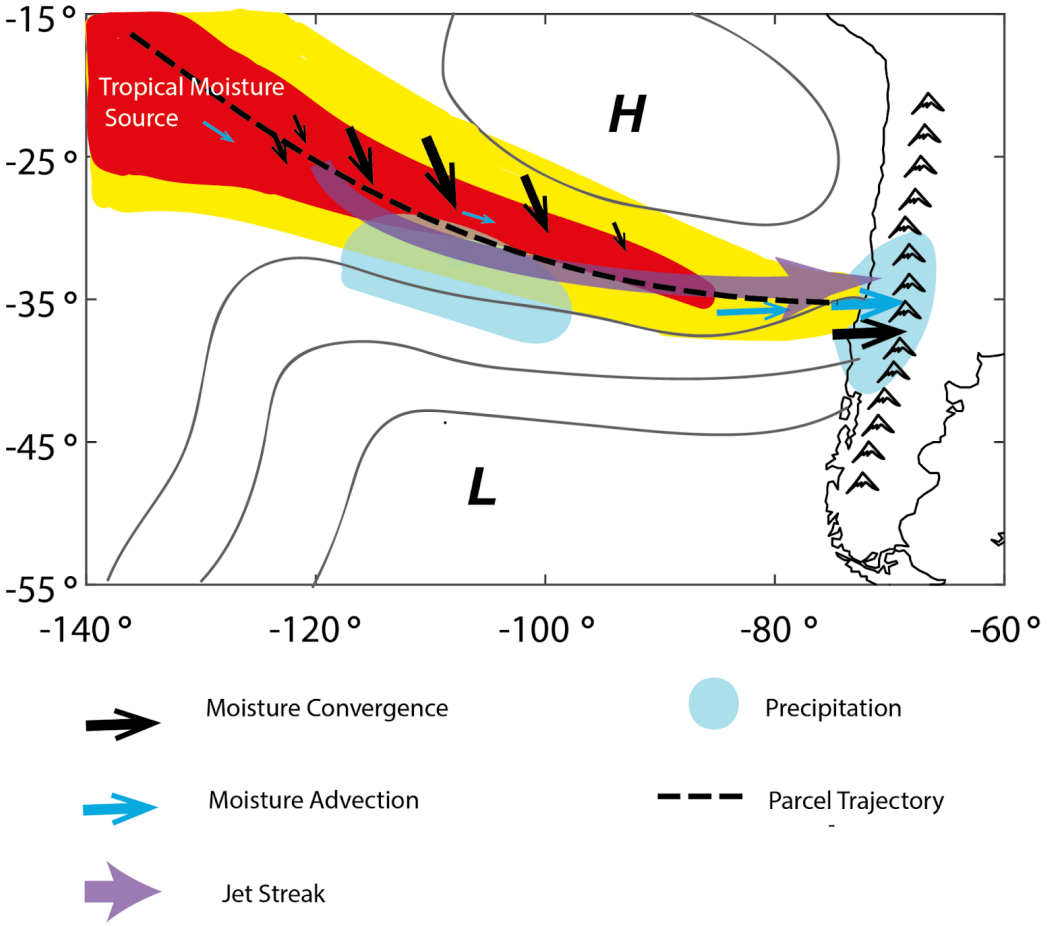

Figure 4: A schematic diagram showing a Lagrangian view (that is a view following a parcel that makes landfall when precipitation increases near the coast) of a typical landfalling atmospheric river in Chile. The shaded areas indicate integrated water vapor (IWV) along the AR channel. The symbols 'H' and 'L' indicate the location of a subtropical anticyclone and a midlatitude trough.

Our results suggest that mass convergence and moisture advection may work in tandem to transport moisture along the AR to the landfalling region, and we speculate that they also feedback among themselves. The primary findings from our analysis are summarized in Figure 4.

In regions of moisture convergence, the compensation between moisture convergence and precipitation implies significant recycling of water vapor. Future numerical and field experiments, involving moisture tagging, water vapor tracing, and isotopic characterization of precipitation, could shed light on the contributions of air masses from different source regions to the landfalling moisture of the AR.

We finally warn that we have selected our 50 ARs based on those that produce significant increases in precipitation upon landfall, and therefore our results are biased by the selection of these cases. In other words, the approximate conservation of IWV and the balance between moisture convergence and precipitation are features of these "successful" rivers. Similar conditions could occur in the tropics but may lack one or some of these ingredients, failing to produce a landfalling AR.

Acknowledgments: This research was partially funded by grant ANID Anillo ACT210046 and FONDAP/ANID (1523A0002) CR2.

Open Research

The ERA5 data at pressure levels and single level can be downloaded from the links https://cds.climate.copernicus.eu/cdsapp#!/dataset/reanalysis-era5-pressure-levels?tab=form and https://cds.climate.copernicus.eu/cdsapp#!/dataset/reanalysis-era5-single-levels?tab=for

m. The AR backward trajectories are obtained from HYSPLIT interactive web platform https://www.ready.noaa.gov/index.php. The matlab code used to select the trajectory and budget calculation can be obtained in https://osf.io/ezc32/. The ARTMIP catalogs used to identify the AR can be obtained from https://www.earthsystemgrid.org/dataset/ucar.cgd.artmip.tier1.catalogues.html.

References:

Bao, J.-W., Michelson, S. A., Neiman, P. J., Ralph, F. M., & Wilczak, J. M. (2006). Interpretation of Enhanced Integrated Water Vapor Bands Associated with Extratropical Cyclones: Their Formation and Connection to Tropical Moisture. *Monthly Weather Review*, *134*(4), 1063–1080.

Campos, D., & Rondanelli, R. (2023). ENSO−related precipitation variability in Central Chile: The role of large scale moisture transport. *Journal of Geophysical Research*. https://doi.org/10.1029/2023jd038671

Dacre, H. F., Clark, P. A., Martinez-Alvarado, O., Stringer, M. A., & Lavers, D. A. (2015). How Do Atmospheric Rivers Form? *Bulletin of the American Meteorological Society*, *96*(8), 1243–1255.

Draxler, R. R., & Rolph, G. D. (2010). HYSPLIT (HYbrid Single-Particle Lagrangian Integrated Trajectory) model access via NOAA ARL READY website (http://ready. arl. noaa. gov/HYSPLIT. php), NOAA Air Resources Laboratory. *Silver Spring, MD*, *25*. Retrieved from https://www.ready.noaa.gov/hysplit_metadata.html

Garreaud, R. D. (2013). Warm Winter Storms in Central Chile. *Journal of Hydrometeorology*, *14*(5), 1515–1534.

Garreaud, R. D. (2023, June 27). Vuelven los gigantes: un análisis preliminar de la

tormenta ocurrida entre el 21 y 26 de junio de 2023 en Chile central. Retrieved February 1, 2024, from https://www.cr2.cl/analisis-cr2-vuelven-los-gigantes-un-analisis-preliminar-de-la-tormenta-ocurrida-entre-el-21-y-26-de-junio-de-2023-en-chile-central/

Garreaud, R. D., Rutllant, J., Quintana, J., Carrasco, J., & Minnis, P. (2001). CIMAR-5: A Snapshot of the Lower Troposphere over the Subtropical Southeast Pacific. *Bulletin of the American Meteorological Society*, *82*(10), 2193–2208.

Guan, B., & Waliser, D. E. (2015). Detection of atmospheric rivers: Evaluation and application of an algorithm for global studies. *Journal of Geophysical Research, D: Atmospheres*, *120*(24), 12514–12535.

Guan, B., Molotch, N. P., Waliser, D. E., Fetzer, E. J., & Neiman, P. J. (2013). The 2010/2011 snow season in California's Sierra Nevada: Role of atmospheric rivers and modes of large-scale variability. *Water Resources Research*, *49*(10), 6731–6743.

Guan, B., Waliser, D. E., & Ralph, F. M. (2020). A multimodel evaluation of the water vapor budget in atmospheric rivers. *Annals of the New York Academy of Sciences*, *1472*(1), 139–154.

Hersbach, H., Bell, B., Berrisford, P., Hirahara, S., Horányi, A., Muñoz−Sabater, J., et al. (2020). The ERA5 global reanalysis. *Quarterly Journal of the Royal Meteorological Society*, *146*(730), 1999–2049.

Luo, Q., & Tung, W.-W. (2015). Case Study of Moisture and Heat Budgets within Atmospheric Rivers. *Monthly Weather Review*, *143*(10), 4145–4162.

Michaelis, A. C., Martin, A. C., Fish, M. A., Hecht, C. W., & Martin Ralph, F. (2021). Modulation of Atmospheric Rivers by Mesoscale Frontal Waves and Latent Heating: Comparison of Two U.S. West Coast Events. *Monthly Weather Review*,

149(8), 2755–2776.

Norris, J. R., Martin Ralph, F., Demirdjian, R., Cannon, F., Blomquist, B., Fairall, C. W., et al. (2020). The Observed Water Vapor Budget in an Atmospheric River over the Northeast Pacific. *Journal of Hydrometeorology*, *21*(11), 2655–2673.

Rutllant, J. A., Matus, F., Rudloff, V., & Rondanelli, R. (2023). The role of atmospheric rivers in rainfall-induced landslides: A study from the Elqui valley. *Journal of Arid Environments*, *216*, 105016.

Sodemann, H., & Stohl, A. (2013). Moisture Origin and Meridional Transport in Atmospheric Rivers and Their Association with Multiple Cyclones. *Monthly Weather Review*, *141*(8), 2850–2868.

Stohl, A., Forster, C., & Sodemann, H. (2008). Remote sources of water vapor forming precipitation on the Norwegian west coast at 60°N-a tale of hurricanes and an atmospheric river. *Journal of Geophysical Research*, *113*(D5). https://doi.org/10.1029/2007jd009006

Valenzuela, R., & Garreaud, R. D. (2019). Extreme Daily Rainfall in Central-Southern Chile and Its Relationship with Low-Level Horizontal Water Vapor Fluxes. *Journal of Hydrometeorology*, *20*(9), 1829–1850.

Valenzuela, R., Garreaud, R., Vergara, I., Campos, D., Viale, M., & Rondanelli, R. (2022). An extraordinary dry season precipitation event in the subtropical Andes: Drivers, impacts and predictability. *Weather and Climate Extremes*, *37*, 100472.

Viale, M., Valenzuela, R., Garreaud, R. D., & Martin Ralph, F. (2018). Impacts of Atmospheric Rivers on Precipitation in Southern South America. *Journal of Hydrometeorology*, *19*(10), 1671–1687.

Zhu, Y., & Newell, R. E. (1998). A Proposed Algorithm for Moisture Fluxes from Atmospheric Rivers. *Monthly Weather Review*, *126*(3), 725–735.